First records of winter sea ice concentration in the southwest Pacific sector of the Southern Ocean

Alexander J Ferry, Xavier Crosta, Patrick G Quilty, David Fink, William Howard, Leanne Armand

AGU PUBLICATIONS

Paleoceanography

RESEARCH ARTICLE
10.1002/2014PA002764

First records of winter sea ice concentration in the southwest Pacific sector of the Southern Ocean

Alexander J. Ferry[1], Xavier Crosta[2], Patrick G. Quilty[3], David Fink[4], William Howard[5], and Leanne K. Armand[1]

[1]Department of Biological Sciences, Climate Futures at Macquarie University, Sydney, New South Wales, Australia, [2]Université de Bordeaux, UMR-CNRS 5805 EPOC, Pessac, France, [3]School of Earth Sciences, University of Tasmania, Hobart, Tasmania, Australia, [4]Institute for Environmental Research, Australian Nuclear Science and Technology Organization, Menai, New South Wales, Australia, [5]School of Earth Sciences, University of Melbourne, Melbourne, Victoria, Australia

Key Points:
- Winter sea ice extent varies over Antarctic Cold Reversal and Holocene
- The southwest Pacific paleo sea ice records contrasts that of the Atlantic
- Describe new age models for core E27-23 and SO136-111

Correspondence to:
L. K. Armand,
leanne.armand@mq.edu.au

Citation:
Ferry, A. J., X. Crosta, P. G. Quilty, D. Fink, W. Howard, and L. K. Armand (2015), First records of winter sea ice concentration in the southwest Pacific sector of the Southern Ocean, *Paleoceanography*, *30*, 1525–1539, doi:10.1002/2014PA002764.

Received 2 DEC 2014
Accepted 2 OCT 2015
Accepted article online 15 OCT 2015
Published online 24 NOV 2015

Abstract We use a Generalized Additive Model (GAM) to provide the first winter sea ice concentration record from two cores located within the southwest Pacific sector of the Southern Ocean. To compliment the application of GAM, a time series analysis on satellite records of sea ice concentration data was used to extend the standard 13.25 year time series used for paleoceanography. After comparing GAM sea ice estimates with previously published paleo sea ice data we then focus on a new paleo winter sea ice record for marine sediment core E27-23 (59°37.1'S, 155°14.3'E), allowing us to provide a more comprehensive view of winter sea ice dynamics for the southwest Pacific Ocean. The paleo winter sea ice concentration estimates provide the first suggestion that winter sea ice within the southwestern Pacific might have expanded during the Antarctic Cold Reversal. Throughout the Holocene, core E27-23 documents millennial scale variability in paleo winter sea ice coverage within the southwest Pacific. Holocene winter sea ice expansion may have resulted from the Laurentide Ice Sheet deglaciation, increased intensity of the westerly winds, as well as a northern migration of the Subtropical and/or Sub-Antarctic Fronts. Brief consideration is given to the development of a paleo summer sea ice proxy. We conclude that there is no evidence that summer sea ice ever existed at core sites SO136-111 and E27-23 over the last 220 and 52,000 years, respectively.

1. Introduction

Sea ice is the most obvious expansive and seasonal geophysical parameter on the Earth's surface [*Comiso*, 2010]. The annual sea ice cycle of formation and retreat influences atmospheric and oceanic processes and therefore modulating the global climate [*Dieckmann and Hellmer*, 2010; *Comiso*, 2010; *Brandon et al.*, 2010]. Sea ice exerts a significant influence on the radiative balance of the polar regions and acts as an insulator limiting ocean-atmosphere heat and gas fluxes [*Comiso*, 2010]. Reconstructing the historical and paleo environmental occurrence of sea ice is a key component of any effort attempting to understand past and future climatic change [*Dieckmann and Hellmer*, 2010].

Diatom abundances are a well-established proxy for Southern Ocean sea ice, providing a means to obtain qualitative [*Gersonde and Zielinski*, 2000; *Schneider-Mor et al.*, 2005] and quantitative estimates for winter (September) sea ice concentrations, as well as monthly sea ice cover [*Crosta et al.*, 1998; *Gersonde et al.*, 2005; *Armand and Leventer*, 2010]. Core SO136-111 (~56°S, 160°E) permitted the first quantitative reconstruction of paleo sea ice over the previous two climatic cycles, documenting glacial to interglacial sea ice advance and retreat during marine isotopic stages 6, 4, and 2 [*Crosta et al.*, 2004].

The paleo sea ice record derived from core SO136-111 has served as a benchmark for the establishment of new Southern Ocean sea ice proxies such as sea salt flux [*Röthlisberger et al.*, 2010], and iodide and iodate speciation deposited within an Antarctic ice core [*Spolaor et al.*, 2013]. The signals recorded within proxy data can constrain hypotheses to be tested by climate models, while climate models can be evaluated by comparison of their output with proxy records. Comparisons between models and proxies provide an opportunity to study mechanisms that may have been important for past sea ice variability but may be of less significance in the modern day climate [*Goosse et al.*, 2013]. Our paleo sea ice records at the locations of cores SO136-111 and E27-23 (59°S, 155°E) provide paleo data against which new proxies and climate models can be validated.

This paper applies a recently developed application of a Generalized Additive Model (GAM) [*Ferry et al.*, 2015] to revise paleo sea ice estimates for core SO136-111. *Ferry et al.* [2015] concluded that GAM was the most robust method for estimating paleo sea ice as it had the lowest prediction error, was the least biased by spatial autocorrelation, and provided the most unbiased paleo sea ice estimates. In applying GAM to core SO136-111 we aim to compare GAM with the Modern Analogue Technique (MAT) of *Crosta et al.* [2004], illustrating the broad consistency between the two methods, as well as the improvement GAM provides the paleo oceanographer.

As the diatom core top samples represent, on average, 1 kyr of sedimentation, it is important that the sea ice training data set excludes the effects of recent decadal climate change. Previous work used the 13.25 year satellite record of *Schweitzer* [1995], which ends in December 1991, to exclude the effects of recent decadal climatic change. However, *Armand and Leventer* [2010] questioned whether the use of a 13.25 year satellite record of sea ice concentration data may be too short for computing an average sea ice concentration value that is representative of the sea ice climatology. We apply a time series analysis on sea ice concentration data to identify residual trends, defined as statistically significant increases or decreases in sea ice concentration over time that cannot be explained by climatic variables (for example, the El Niño–Southern Oscillation) or seasonal (and decadal) variations in sea ice concentrations. Excluding that portion of the satellite sea ice concentration record in which such trends can be identified may assist in the estimation of climatologically representative sea ice concentrations for our training data set.

We then provide the first paleo winter sea ice records for cores SO136-111 and E27-23, expanding the paleo sea ice record of the southwest Pacific sector of the Southern Ocean to include seasonality. We compare our sea ice records for the southwest Pacific sector with paleo sea ice records from the South Atlantic sector of the Southern Ocean [*Bianchi and Gersonde*, 2004; *Divine et al.*, 2010]. Core E27-23, compared to core SO136-111, is located closer to the modern winter sea ice edge in a position that is more analogous to the Atlantic cores. Therefore, core E27-23 allows us to provide a more robust comparison between the paleo sea ice record from southwest Pacific and Atlantic sectors of the Southern Ocean over the last 15 kyr BP. Our focus then shifts to the southwest Pacific over last 15 kyr BP, focusing on the Antarctic Cold Reversal (ACR) and Holocene millennial scale climatic changes.

2. Methods

2.1. Training and Core Data Sets

We use 163 seafloor samples from the 243 samples present within the training database of *Crosta et al.* [2004] to estimate winter paleo sea ice concentrations (Figure 1). Each of the seafloor samples documents the relative abundance of 32 diatom species. The original training data set included many open ocean samples used to estimate sea surface temperature; the inclusion of which, for the purposes of sea ice estimation, would have been redundant. We chose to exclude some samples to establish a more even sampling of the environmental gradient within our training data set [*Telford and Birks*, 2011]. Exclusion of samples was also carried out with respect to the spatial structure of our data so that no single geographic locality was overrepresented or underrepresented within our training set. Thus, our objective was to remove samples from a broad range of longitudinal and latitudinal bands in order to preserve spatial diversity. Sea ice concentration data were derived from the bootstrapped algorithm of *Comiso* [2000] and supplied by the National Snow and Ice Data Centre. Winter sea ice concentration (wSIC) was defined as the September average sea ice concentration [*Gersonde et al.*, 2005]. Sea ice concentration is defined as that fraction, or percentage, of ocean area that is covered by sea ice [*Cavalieri et al.*, 1996]. All marine isotope stages (MIS) are defined according to *Lisiecki and Raymo* [2005a, 2005b]. We define the extended Last Glacial Maximum (eLGM) as that period between 35 and 18 kyr B.P. [*Newnham et al.*, 2007], while the timing for the Antarctic Cold Reversal (ACR) is 14.2 to 12.5 kyr B.P. [*Weber et al.*, 2014].

Core SO136-111 [*Crosta et al.*, 2004] was collected from 56°40′S, 160°14′E within the Emerald Basin and Polar Frontal Zone (southwest Pacific sector of the Southern Ocean) (Figure 1). The core preserves a record of the last 200 kyr. However, as the core top is missing, the record of paleo sea ice cover ends during the late Holocene at ~3 kyr B.P. Sediment core E27-23 was extracted from 59°37.1′S, 155°14.3′E from a water depth of 3182 m [*Cassidy et al.*, 1977]. The core chronology is presented hereafter for the first time. Both cores are situated south of the Sub-Antarctic Front within the Antarctic Circumpolar Current (ACC), with E27-23 located closer to the modern winter sea ice edge than core SO136-111 (Figure 1).

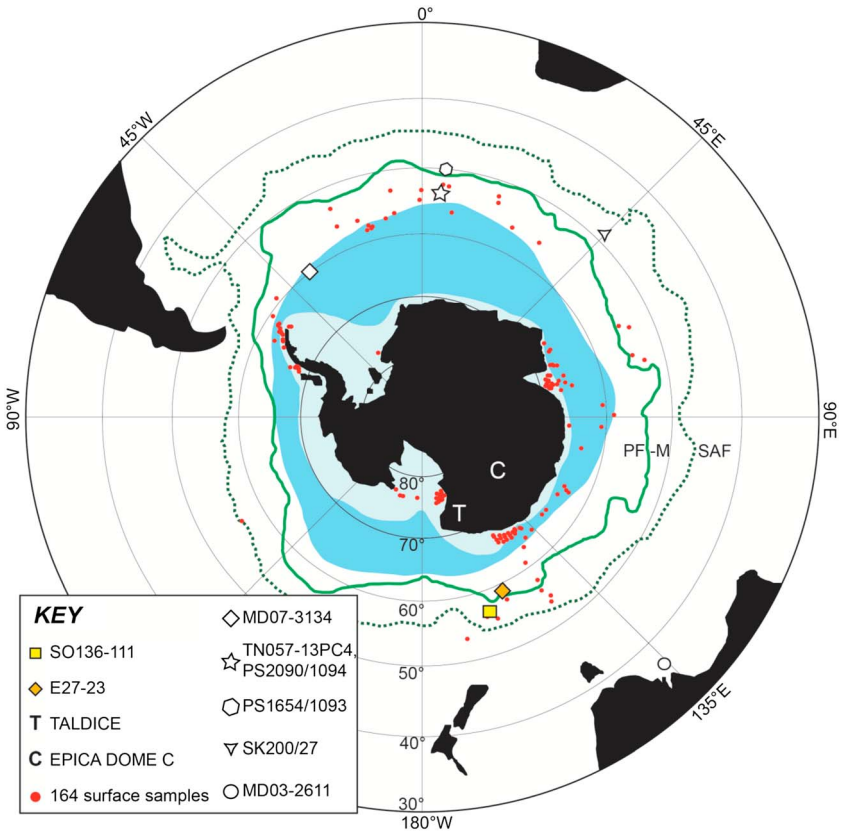

Figure 1. The locations of the 163 samples used in our training data base (red circles) with the winter sea ice edge (light blue shaded area) and summer sea ice edge (pale blue shaded area). Also shown for context are the mean locations for the Polar Front (PF-M; green line) and the Sub-Antarctic Front (SAF; dashed green line) [*Sokolov and Rintoul*, 2009]. Locations for the TALDICE and EPICA Dome C ice cores and marine sediment cores SO136-111, E27-23 (from the southwest Pacific), TN057-13PC4, PS2090/1094, and PS1654/1093 (from the Atlantic) are also indicated. (Cores SK200/27 [*Manoj et al.*, 2013] and MD07-3134 [*Weber et al.*, 2014], used to examine IBRD records, are identified.)

2.2. Analysis of the Sea Ice Data Time Series

While Antarctic sea ice extent as a whole has been increasing over the last 35 years, it is still important to investigate sea ice behavior on a regional scale [*Stammerjohn et al.*, 2012; *Parkinson and Cavalieri*, 2012; *Massom et al.*, 2013; *Simmonds*, 2015]. We analyzed the satellite record separately for each sector (as defined by *Gloersen et al.* 1992]) of the Southern Ocean. We applied an Auto Regressive Integrated Moving Average (ARIMA) model to the sea ice satellite record, sourced via the bootstrapped algorithm of *Comiso* [2000], from November 1978 to December 2010. The ARIMA model was fitted using the forecast package for R, version 4.01 [*Hyndman*, 2014]. The input series (covariates) included within our ARIMA included the following: the multivariate El Niño–Southern Oscillation Index (MEI), the Southern Annular Mode (SAM), the Antarctic Oscillation (AAO), the average monthly CO_2 concentrations for Mauna Loa, the Total Solar Irradiance Index at Earth distance in W/m^2 (TSI), average monthly maximum temperatures, and the Southern Hemisphere Land-Ocean Temperature Index (LOTI).

AAO data were sourced from the National Oceanic and Atmospheric Administration's (NOAA) national weather service, climate prediction center. MEI is provided by the NOAA physical sciences division. TSI data are published by the University of Colorado, Boulder SORCE experiment. SAM data were compiled by the British Antarctic Survey, and month/yr average CO_2 was sourced from NOAA ESRI data.

We focused our analysis on two sea ice concentration data sets. The first represents a winter average sea ice concentration calculated from 13.25 years of satellite data, consistent with the methodology of *Crosta et al.* [2004]. The second sea ice concentration data set uses average sea ice concentrations calculated from an extended time series of satellite data. The exact temporal extent of the satellite data used is unique to each sector of the Southern Ocean and defined by our time series (ARIMA) modeling.

2.3. Reconstruction Diagnostics

We compare the maximum recorded diatom abundances between our training set and the fossilized assemblages of marine sediment cores SO136-111 and E27-23. Hills N2 diversity index [*Hill*, 1973] was used to identify the effective number of occurrences for each diatom species within the training data set and therefore to identify species that may have poorly defined optima. Analog quality, and the presence of no analog samples for cores SO136-111 and E27-23, was explored with a squared chord distance and the five closest analogs. Regarding analog quality, those samples considered to have no analog had a distance greater than the 5th percentile of all distances computed between the training and core data sets, while samples with poor analogs had a distance between the 10th and 5th percentiles of all distances. Examination of analog quality, and the presence of no analog samples, not only is relevant for MAT but also is important to consider when applying all methods for the reconstruction of paleo sea ice. Sea ice estimations derived from all reconstruction methods on core samples with poor analogs need to be treated with caution. A canonical correspondence analysis constrained by wSIC was used to compute a squared residual length for the taxonomic distances between the winter sea ice axis and the samples within our training data set and the cores SO136-111 and E27-23. A core sample, with a squared residual length exceeding the 90th percentile for the squared residual lengths computed on the training set, is regarded as poorly fitted by winter sea ice concentrations [*Hill*, 1973; *Birks et al.*, 1990].

2.4. The Statistical Models Used

Our paleo winter sea ice data were estimated with a new application of GAM [*Ferry et al.*, 2015]. The absence of diatom flux to the seafloor is considered to provide a proxy for permanent sea ice cover and, by extension, the presence of summer sea ice [*Gersonde et al.*, 2005]. We therefore examined the presence of diatoms recorded in each core to infer the potential presence of summer sea ice cover at the sites of core SO136-111 and E27-23. We used the statistical software PAST [*Hammer et al.*, 2001] to apply MAT. We used the package mgcv [*Wood*, 2014] to apply GAM and rioja [*Juggins*, 2014] to apply the reconstruction diagnostics. Following *Gloersen et al.* [1992] and *Gersonde et al.* [2005], we consider wSIC less than 15% to indicate no sea ice cover, 15 to 40% represents unconsolidated sea ice, and concentrations above 40% to represent consolidated winter sea ice. MAT estimates equal to or above an average of 1 month of sea ice coverage per year are regarded as an indicator for the presence of sea ice.

2.5. Material and Stratigraphy

2.5.1. E27-23 Chronology

A chronostratigraphy for piston core E27-23 (59°37.1'S, 155°14.3'E, water depth 3182 m) was established principally from Accelerator Mass Spectrometry (AMS) radiocarbon dating. Samples of the planktonic foraminifer *Neogloboquadrina pachyderma* sinistral were ultrasonically cleaned in methanol and oven dried at 60°C prior to analysis. Twenty-six AMS ^{14}C measurements were made at the Australian Nuclear Science and Technology Organization (ANSTO) using the ANTARES accelerator facility [*Fink et al.*, 2004]. The conversion of foraminiferal calcite to CO_2 at ANSTO used a reaction with 85% phosphoric acid. H2/Fe catalytic reduction then converted the gas to graphite [*Hua et al.*, 2001]. A Micromass IsoPrime EA/IRMS at ANSTO measured δ^{13}C from the graphite of each sample, with a range of -0.5 to -3‰. When sample sizes were too small to allow δ^{13}C measurement to be made on the graphite, a value of 0% was assigned for the purposes of radiocarbon age calculation, consistent with the δ^{13}C of foraminiferal calcite being close to that of seawater δ^{13}C-DIC. Six AMS ^{14}C measurements, following a similar method at the National Ocean Sciences Accelerator Mass Spectroscopy facility (Woods Hole, Massachusetts, USA), were added to the ANSTO AMS ^{14}C measurements [*Anderson et al.*, 2009; Burckle, personal communication; Appendix A: doi:10.4225/15/546C10AD26A7D] to construct an age model.

Ten AMS ^{14}C measurements were discarded because they were outliers or presented age reversals (Appendix A: doi:10.4225/15/546C10AD26A7D). All remaining AMS dates were converted to calendar ages using the linear-based CALIB07 [*Stuiver and Reimer*, 1993] with calibration to the Marine13 data set [*Reimer et al.*, 2013] at 95.4% confidence (2 sigma) and included a correction for the surface water reservoir age of ~752 years at the site of core E27-23 resolved from the marine radiocarbon reservoir correction database and software available from http://radiocarbon.LDEO.columbia.edu/ [*Butzin et al.*, 2005]. For comparison, we also used OXCAL 4.2 [*Bronk Ramsey,* 2009; *Blaauw,* 2010], to calibrate the dates with the same curve and surface reservoir age and found <5 years difference between the calibrated ages for ages younger than 30 kyr B.P. The greatest calibration offset was 40 years at our only sample older than 35 kyr B.P. (Appendix B:

Table 1. Final Age Model Tie Points Used to Determine the Age Model for E27-23[a]

Midpoint Depth (cm)	Tie Point Method used	Final Age Model Tie Point (cal years BP)
1	Sed. rate CALIB07 + LR04	1472
3	Sed. rate CALIB07 + LR04	1541
4.0	^{14}C AMS CALIB07	1576
26.5	^{14}C AMS CALIB07	2132
32.5	^{14}C AMS CALIB07	2167
103.0	^{14}C AMS CALIB07	5136
199.0	^{14}C AMS CALIB07	6030
299.0	^{14}C AMS CALIB07	6786
379.0	^{14}C AMS CALIB07	7510
439.0	^{14}C AMS CALIB07	8073
509.0	^{14}C AMS CALIB07	10201
529.0	^{14}C AMS CALIB07	10946
589.0	^{14}C AMS CALIB07: Av. 579 and 599 cm	13025
600.5	^{14}C AMS CALIB07	13268
619.0	^{14}C AMS CALIB07	13584
629.0	^{14}C AMS CALIB07	14596
639.0	^{14}C AMS CALIB07	15586
719.0	^{14}C AMS CALIB07	16785
760.5	^{14}C AMS CALIB07	17138
779.0	^{14}C AMS CALIB07	17337
780.5	^{14}C AMS CALIB07	21136
799.0	^{14}C AMS CALIB07	27759
849.0	^{14}C AMS CALIB07	35271
879.1	δ^{18}O tuning LR04-Linage	45126
899.0	δ^{18}O tuning LR04-Linage	48969
948.8	δ^{18}O tuning LR04-Linage	51905

[a]Calibrated ages principally represent calibrated ages from ^{14}C AMS dates using CALIB07. Alternate methods were used to determine ages where ^{14}C AMS dates were not obtained. Three tie points (between 849 and 949 cm) were determined by calibrating the $\delta^{18}O_{Nps}$ to the Lisiecki and Raymo benthic δ^{18}O stack [*Lisiecki and Raymo,* 2005a, 2005b] (δ^{18}O tuning LR04) applying Analyseries 2.0.8 [*Paillard et al.,* 1996]. Core top ages (0–4 cm) were determined from a linear extrapolation of the estimated sedimentation rate at the top of the core. Additional information is provided in Appendix A (doi:10.4225/15/546C10AD26A7D).

doi:10.4225/15/546C10AD26A7D). For the sake of consistency with other palaeoceanographic records in this region, we have retained the CALIB07 calibrated AMS ages for the construction of our chronostratigraphy. Due to the nearly identical AMS dates obtained at 579 and 599 cm (13,020 and 13,029 cal years B.P., respectively) we have averaged the depths and ages to provide a single tie point (589 cm, 13,024.5 cal years B.P.) (Table 1).

To supplement the 21 AMS calibrated ages, we also measured the oxygen isotopes (expressed as δ^{18}O) on planktonic foraminifera *N. pachyderma* (sinistral; >150 μm). The foraminiferal samples were cleaned as described for the radiocarbon analysis above. Measurements of δ^{18}O were made on a Finnigan MAT 251 isotope ratio mass spectrometer with an automated individual carbonate reaction ("Kiel") device at the Australian National University. The samples, weighing between 59 and 221 μg, were reacted with 105% phosphoric acid for 13 min at 90°C. Isotope values are reported as per mil (‰) deviations relative to the Vienna Peedee belemnite (VPDB) (Appendix C: doi:10.4225/15/546C10AD26A7D) and calibrated via the National Bureau of Standards carbonate standard NBS-19. Analytical precision (2 sigma) for NBS-19 standards, run with these samples, was ±0.07 ‰ for δ^{18}O and ±0.03 ‰ for δ^{13}C ($n = 39$).

Three tie points for the deepest section of the core (849–949 cm) were used to correlate our δ^{18}O record to the global composite benthic δ^{18}O record LR04 [*Lisiecki and Raymo,* 2005a, 2005b] (Table 1, Figure 2) applying the "Linage" subroutine of Analyseries 2.0.8 [*Paillard et al.*, 1996]. Although a recent benthic δ^{18}O global overview was compiled by *Stern and Lisiecki* [2014], data coverage throughout the south Pacific sector of the Southern Ocean was absent, hindering their ability to evaluate the variability in the timing of the δ^{18}O response [*Stern and Lisiecki*, 2014]. Therefore, our chronology used the δ^{18}O record of *Lisiecki and Raymo* [2005a, 2005b]. Our accepted calibrated AMS ages were used as additional tie points during this process. In contrast, to determine the core top ages (0–4 cm), we used a linear extrapolation of the estimated

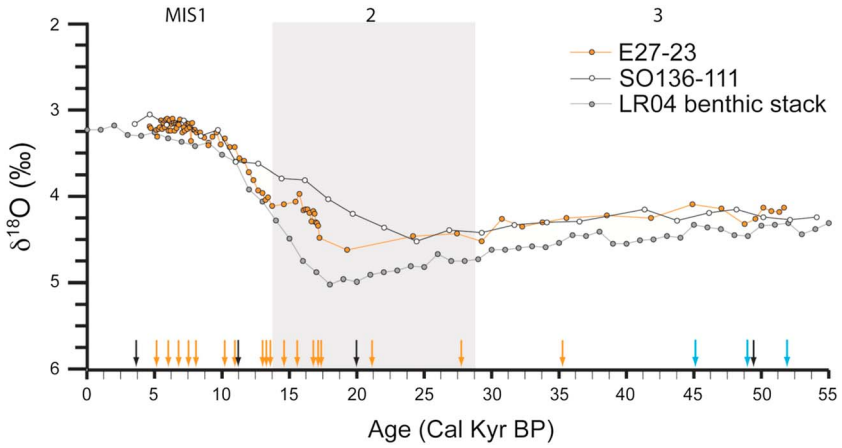

Figure 2. Age calibrated δ^{18}O isotope curve comparison between the δ^{18}O (*Neogloboquadrina pachyderma* sinistral (planktic)) from E27-23 and SO136-111, and the global benthic δ^{18}O stack [LR04; *Lisiecki and Raymo,* 2005a, 2005b]. Arrows indicate the calibrated ^{14}C AMS age pointers from E27-23 (orange) and SO136-111 (black) used to correlate to the global benthic stack. Three additional correlation tie points (Table 1, blue arrows) for the core E27-23 are based on a direct correlation between E27-23 and the LR04 benthic stack.

sedimentation rate (34.8 cm/kyr) near the top of the core. Our final age model for core E27-23 is based on 26 tie points, of which 21 are calibrated ^{14}C dates (Table 1, Figure 3).

2.5.2. SO136-111 Chronology

Details regarding the original age model of gravity core SO136-111 (56°40′S, 160°14′E, water depth 3912 m) have been provided elsewhere [*Crosta et al.*, 2002, 2004, 2005]. In this paper, we have revised the age model to duplicate the same chronostratigraphic process applied to E27-23. We have recalibrated the original ^{14}C dates [*Crosta et al.*, 2004] using the CALIB07 software and Marine13 data set [*Stuiver and Reimer*, 1993; *Reimer et al.*, 2013] at 95.4% confidence. Due to the more northerly location of SO136-111, a slightly lower surface water reservoir age of ~623 years was derived from the marine radiocarbon reservoir correction database and applied to the calibration model (http://radiocarbon.LDEO.columbia.edu/) [*Butzin et al.*, 2005]. The δ^{18}O planktonic foraminifera record was tuned to the LR04 stack [*Lisiecki and Raymo,* 2005a, 2005b] using Analyseries 2.0.8, to provide additional tie points beyond the radiocarbon time frame. Thus, both calibrated ^{14}C and δ^{18}O tie points (Appendix D: doi:10.4225/15/546C10AD26A7D) serve to provide a refined and comparable age model for SO136-111 (Figure 2). We acknowledge that our preference for relying on the ^{14}C tie points over the δ^{18}O tuning to the LR04 stack leads to a less than satisfactory match for the deglaciation records presented here in contrast to the longer time series that the core SO136-111 represents overall. However, we feel it is sounder to rely on the ^{14}C dates rather than planktonic δ^{18}O tuning, as planktonic δ^{18}O data can be impacted by factors such as the vertical migration of foraminifera and regional hydrographic effects altering planktonic foraminifera δ^{18}O, of which in this region of the Southern Ocean there have been no studies to determine the impact of such effects.

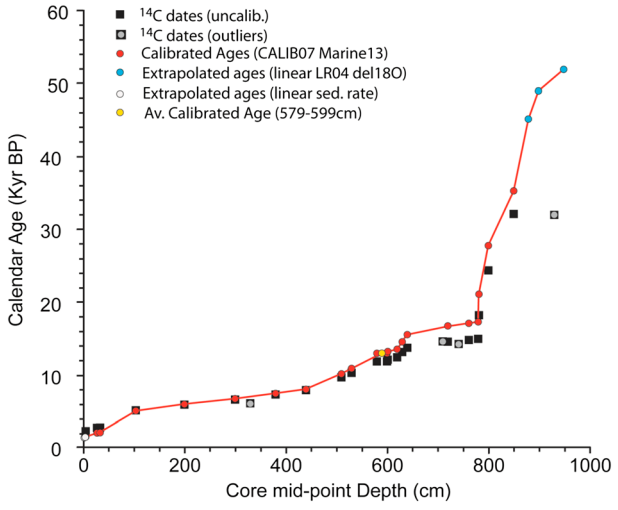

Figure 3. Derivation of the E27-23 depth-age model. Included within the figure are the raw ^{14}C AMS dates (black squares) including outliers (black squares with grey dots); CALIB07 Calibrated Ages from non-outlier dates (red dots and line); with superimposed averaged calibrated age at 589 cm (yellow dot) and additional ages based on correlation to the LR04 benthic δ^{18}O stack (blue dots) and extrapolated linear sedimentation rates (white dots).

Table 2. A Summary of the Final ARIMA Results for Each Sector of the Southern Ocean[a]

Sector [*Gloersen et al.,* 1992]	Significant Climate Indices	Trend Identified	Time Series With No Significant Trend
Weddell Sea	SAM, CO_2	None	November 1978 to December 2010
West Pacific Ocean	Monthly average maximum temperature, CO_2	None	November 1978 to December 2010
Indian Ocean	MEI, Monthly average maximum temperature	None	November 1978 to December 2010
Ross Sea	MEI	Positive	November 1978 to December 1996
Bellingshausen Amundsen Sea	MEI	Negative	November 1978 to December 2006

[a]All significant climatic indices (southern annular mode (SAM) and El Niño Southern Oscillation Index (MEI)) and identified sector trends in sea ice cover are provided. The final sector specific time series, where no trend in sea ice concentrations could be identified are listed.

3. Results

3.1. Sea Ice Time Series Analysis

Based on the final ARIMA models fitted and the trends in sea ice concentration subsequently identified, we found that the full satellite record (32 years) can be used when computing average winter sea ice concentrations for the seafloor diatom assemblage samples located within the Indian Ocean, west Pacific Ocean, and the Weddell Sea sectors of the Southern Ocean. The calculations of winter sea ice averages were restricted to the year 1995 for the samples located within the Ross Sea (17 years), and to 2005 for samples within the Bellingshausen/Amundsen Sea sector (27 years) (Table 2). The calibration assumes that the modern day satellite sea ice record is representative of the last 1000 years represented by each of the core tops within the *Crosta et al.* [2004] training database. The resultant winter sea ice data we use within our training data set accounts for the sector specific changes in sea ice cover, and is therefore more representative than the data set previously used [*Crosta et al.*, 2004].

3.2. Reconstruction Diagnostics

Two diatom species had higher-maximum abundances in core SO136-111 than within our training set, while six species had higher abundances within core E27-23 than in the training set. No species with poorly defined optima were abundant within either core. Of the 164 samples within core SO136-111, only one sample had no analog (at ~201 kyr B.P.), while another eight samples had poor analogs (Figure 4a, Appendix E: doi:10.4225/15/546C10AD26A7D). Core E27-23 had 16 samples with no analog and 39 samples with poor analogs (Figure 5, Appendix F: doi:10.4225/15/546C10AD26A7D). A canonical correspondence analysis, constrained by wSIC, suggests that 31 samples (at ~123-124, 115-121, 7, and 4 kyr B.P.) from core SO136-111 had a squared residual length that exceeded the 90th percentile for the squared residual lengths computed on the training set. Core E27-23 had 17 samples (at ~10, 9.2, 7.5 and 4.6 kyr B.P.) exceeding the 90th percentile for the squared residual lengths computed on the training set.

3.3. Attributes of the wSIC Generalized Additive Models

We herein refer to the GAM used to estimate wSIC calculated from 13.25 years of satellite sea ice concentration data as GAM/WSI/13. We found *Actinocyclus actinochilus*, *Fragilariopsis curta*, *Fragilariopsis cylindrus*, and *Thalassiosira lentiginosa* to be statistically significant proxies for average wSIC computed from 13.25 years of data [*Ferry et al.*, 2015]. The GAM fitted to the wSIC averages calculated from our Extended Time Series satellite record (herein referred to as GAM/WSI/ETS) used the same diatom proxies as GAM/WSI/13. Table 3 summarizes both of the GAM's fitted to our wSIC training data sets.

3.4. GAM Versus MAT Paleo Sea Ice Records

The paleo wSIC estimates provided by GAM/WSI/ETS (Figure 4a) and GAM/WSI/13 (Figure 4b) are both consistent with each other, revealing an average estimate difference of 1.06% and never $>$10% concentration over the last 220 kyr B.P. (Figure 4c). However, as GAM/WSI/ETS is likely to be more climatologically representative given the longer satellite record used to compute an average wSIC, we focus our discussion on the paleo wSIC estimates of GAM/WSI/ETS. GAM/WSI/ETS estimated consolidated winter sea ice at 191, 179, 176, and 171 kyr B.P., while MAT estimated an absence of sea ice (Figure 4d). At 38, 37.5, 23, and 22 kyr B.P., over the eLGM, GAM/WSI/ETS suggests unconsolidated winter sea ice was present over SO136-111 while, similarly, MAT records an increase in monthly sea ice cover. During early MIS 3 (59 to 47 kyr B.P.) GAM/WSI/ETS suggests winter sea ice was absent while MAT estimates the presence of sea ice cover. Both MAT and GAM/WSI/ETS indicate sea ice coverage over the eLGM period, with GAM/WSI/ETS estimating occasional

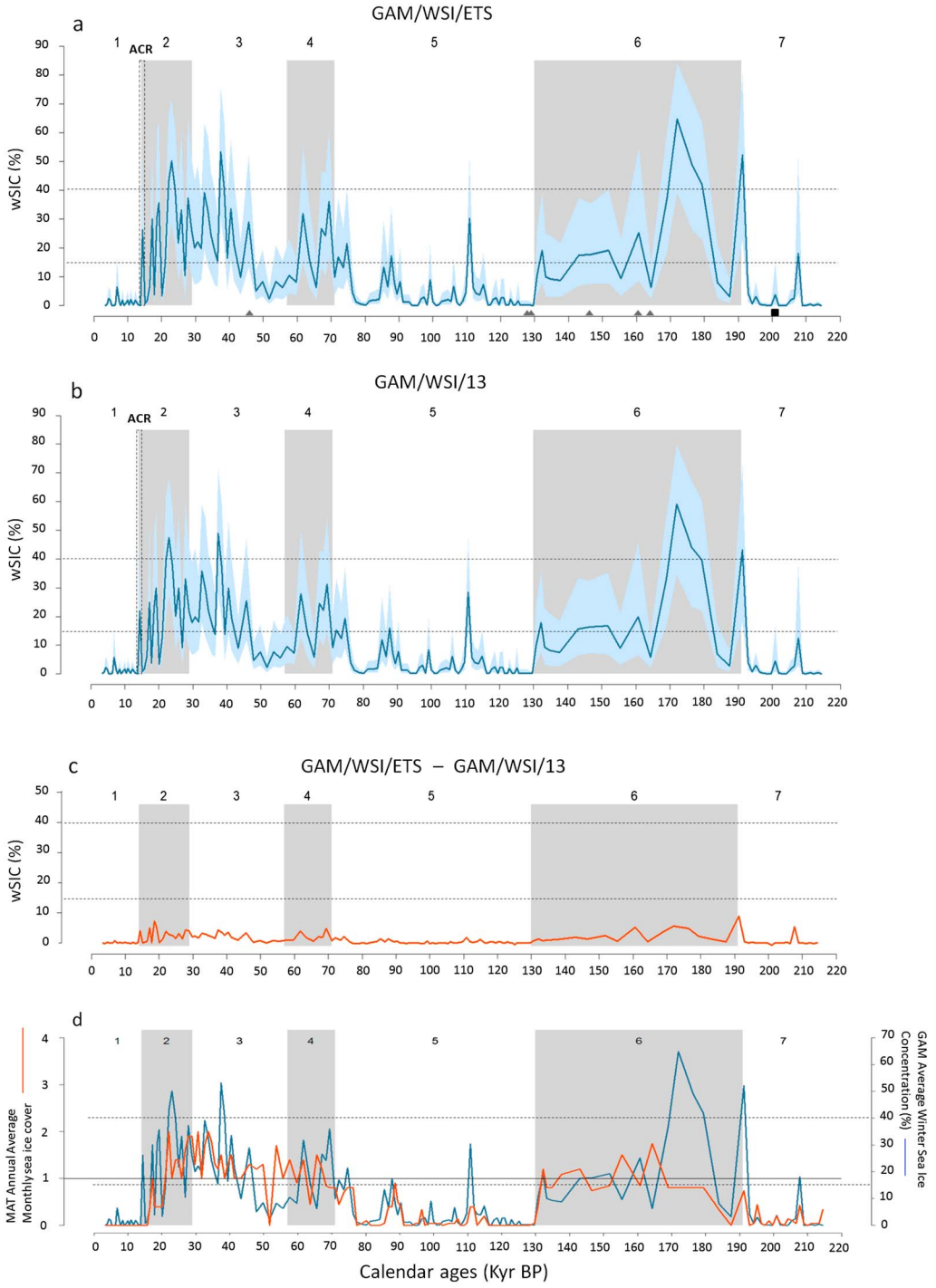

Figure 4. Paleo wSIC estimates determined for core SO136-111. Shown are the estimates from (a) GAM/WSI/ETS and (b) GAM/WSI/13. (c) The difference in wSIC estimates between GAM/WSI/ETS and GAM/WSI/13. The solid blue line indicates the paleo wSIC % concentration estimate, while the light blue shading corresponds to a 95% confidence interval. The dashed box in Figures 4a and 4b highlights the Antarctic Cold Reversal, while in Figure 4a, the solid black square inside the *x* axis highlights no analog samples while the grey triangles highlight samples with poor analogs. All of the marine isotopic stages (1 to 7) are labeled with the glacial marine isotope stages shaded grey. (d) MAT paleo month/yr sea ice cover estimates from *Crosta et al.* [2004] (solid orange line) for SO136-111, contrasted against the wSIC estimates from GAM/WSI/ETS (solid blue line). Estimates of wSIC less than 15% to indicate no sea ice cover, 15 to 40% represent unconsolidated sea ice, while concentrations above 40% represent consolidated winter sea ice (all shown with dashed black horizontal lines) [*Gloersen et al.,* 1992]. MAT estimates equal to or above an average of one month of sea ice coverage (shown by a solid grey horizontal line) per year are regarded as an indicator for the presence of sea ice.

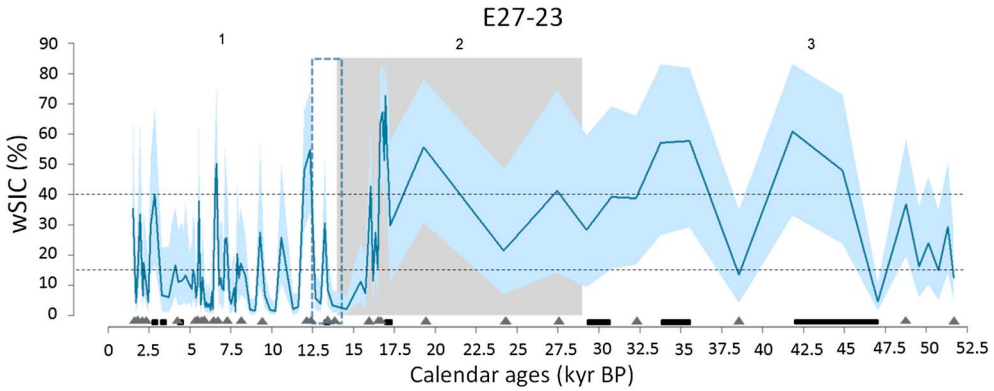

Figure 5. GAM/WSI/ETS model estimates of paleo winter sea ice concentration from core site E27-23. The blue line indicates the paleo wSIC% estimate, while the light blue shading corresponds to a 95% confidence interval. The dashed blue rectangle corresponds to the ACR. The solid black rectangles on the *x* axis highlight those core samples for which there were no analogs, while the grey triangles highlight those samples with poor analogs. All marine isotopic stages are labeled, with the glacial marine isotope stage 2, shaded grey.

consolidated winter sea ice coverage. During the ACR, only GAM/WSI/ETS suggests the winter sea ice edge was present over core SO136-111. Throughout the Holocene, GAM/WSI/ETS and MAT-based estimates indicated no sea ice cover. Henceforth, we interpret our results using GAM derived estimates primarily because the method provides a winter sea ice concentration value, which is of greater utility than estimates of average annual monthly sea ice cover for climate models. Second, we believe GAM is less biased by spatial autocorrelation, provided a better fit to our training data set, and has a stronger biological basis [*Ferry et al.*, 2015].

3.5. The Paleo Sea Ice Record

3.5.1. Paleo Sea Ice Record for Core SO136-111

The site of core SO136-111 generally records wSIC during glacial stages and an absence of winter sea ice during interglacials (Figure 4 and Appendix E: doi:10.4225/15/546C10AD26A7D). Consolidated wSIC seems to have been present between about 180 and 170 kyr B.P. during MIS 6, and may have been sporadically present in the later stages of MIS 3 and in MIS 2. Unconsolidated wSIC may have been briefly present for some intervals during MIS 5 at the site of core SO136-111 at 110, 87, 74, and 72 kyr B.P. From 59 to 47.7 kyr B.P., during the end of MIS 4 and early MIS 3, there was no winter sea ice coverage at the site of core SO136-111. Unconsolidated winter sea ice was estimated during the eLGM from 35 to 27 kyr B.P., and from 25.8 to 21 kyr B.P. An isolated increase in wSIC at 14.5 kyr B.P. corresponds with the ACR, after which (during the Holocene) no winter sea ice cover is estimated for the remainder of the core record. We acknowledge that the 95% confidence intervals for all estimates of unconsolidated and consolidated winter sea ice are large (Figures 4a and 4b), which hinders our ability to confidently discriminate between consolidated and unconsolidated winter sea ice cover. The samples of core SO136-111 provided a continuous down core record of diatom fossils, suggesting the site of core SO136-111 was not covered by consolidated summer sea ice.

Table 3. A Summary of the GAMs Used to Estimate Paleo wSIC[a]

Model	Adjusted R^2	Diatom Proxies	*p* Value
GAM/WSI/13	0.73	*Actinocyclus actinochilus*	0.0027
		Fragilariopsis curta	0.0000000002
		Thalassiosira lentiginosa	0.00172
		Fragilariopsis cylindrus	0.00886
GAM/WSI/ETS	0.716	*Actinocyclus actinochilus*	0.00322
		Fragilariopsis curta	0.0000000003
		Thalassiosira lentiginosa	0.00205
		Fragilariopsis cylindrus	0.01496

[a]Each applied GAM differs according to the satellite sea ice database used to compute average sea ice concentrations for our 163 diatom relative abundance samples. The diatoms used in each of the final models as predictors for a given sea ice cover are listed along with their *p* values.

3.5.2. Paleo Sea Ice Record for Core E27-23

During MIS 3 and 2, E27-23 generally had a wSIC of between 20 and 50%, indicating sporadic consolidated winter sea ice cover. Consolidated Holocene winter sea ice may have reached the core site at 12.3 to 11.9 and 6.8 to 6.5 kyr B.P. Unconsolidated winter sea ice was estimated at 13.2, 10.5, 9.3, 7.8, 6.5, and 2.8 to 2.6, 1.9, and 1.5 kyr B.P. (Figure 5, Appendix F: doi:10.4225/15/546C10AD26A7D). Again, the 95% confidence intervals for all estimates of unconsolidated and consolidated winter sea ice are large (Figure 5), hence we tentatively discriminate between consolidated and unconsolidated winter sea ice cover. As all of the samples from core E27-23 documented the presence of diatoms we conclude the core was never covered by consolidated summer sea ice.

4. Discussion

4.1. The Paleo Winter Sea Ice Records From Cores SO136-111 and E27-23

Our paleo estimates represent an expansion of unconsolidated winter sea ice to 56°S, south of the Tasman Sea, during glacial stages. Others have inferred that the expansion of winter sea ice was a factor in the oceanic fronts of the ACC and the STF migrating north [*Neil et al.*, 2004; *Martinson*, 2012], our work now provides the latitudinal evidence for increased winter sea ice coverage at the sites of E27-23 and SO136-111. Our discussion is initiated by focusing on the glacial and deglacial winter sea ice record from the southwest Pacific sector of the Southern Ocean, outlining the differences in reported sea ice advances from previous records originating in the Atlantic sector [*Bianchi and Gersonde*, 2004; *Divine et al.*, 2010]. The remainder of our discussion is directed toward developing a regional synthesis for the southwest Pacific paleo winter sea ice record over the last 15 kyr B.P., representing sea ice advance during the ACR and the Holocene from the higher-resolution record provided by core E27-23. We link our paleo winter sea ice data with additional oceanographic, ice core, and terrestrial paleo proxy records to place our regional sea ice synthesis in context to hemispheric-scale climate change.

4.1.1. Glacial/Interglacial Variation in Winter Sea Ice Cover

The increase and associated decrease in wSIC between glacial and interglacial climates may be driven by oceanic and atmospheric changes. For instance, the intensity of the Antarctic Circumpolar Current (ACC) and westerly wind field may increase, while migrating to northern latitudes, during glacial stages [*Shulmeister et al.*, 2004; *Mazaud et al.*, 2010; *Kohfeld et al.*, 2013], which effectively expands the atmospheric polar cell, cools the ocean surface and facilitates sea ice expansion in the Southern Ocean [*Putnam et al.*, 2010].

Although the Campbell Plateau provides a bathymetric control on the ACC's position within the southwest Pacific [*Neil et al.*, 2004], it has been argued that the northern extension of paleo sea ice implies a release of the ACC from bathymetric control [*Martinson*, 2012]. Similarly, it has been suggested that the westerly winds migrated north during glacials [*Neil et al.*, 2004; *Putnam et al.*, 2010] however, the discrepancy between model and paleo data based inferences of past westerly wind intensity and latitudinal positioning remains unexplained [*Kohfeld et al.*, 2013]. Our cores, E27-23 and SO136-111, clearly reveal that during glacial stages unconsolidated winter sea ice persisted out to 56°S in the Southern Ocean to the south of the Tasman Sea. These new results provide evidence to previous studies where the expansion of winter sea ice was implicated in the northerly migration of ACC fronts and the STF [*Neil et al.*, 2004; *Martinson*, 2012]. Whether the fronts of the AAC could be, or were, mobile seasonally still remains unresolved.

4.1.2. The Deglacial and Antarctic Cold Reversal

The Antarctic Cold Reversal (ACR) refers to a period of climatic cooling between 14.5 and 12.5 kyr B.P., which interrupted the transition from the Last Glacial Maximum into deglacial conditions [*Stenni et al.*, 2001; *Divine et al.*, 2010]. The ACR has been previously identified from variations to ice rafted debris [*Manoj et al.*, 2013; *Weber et al.*, 2014] (Figures 6d and 6e), δ^{18}O data from the TALDICE ice core [*Stenni et al.*, 2010] (Figure 6f), opal flux records within the south Atlantic [*Anderson et al.*, 2009] and from diatom assemblages within lake sediments of southern South America [*Recasens et al.*, 2015]. Regionally, SST's south of Australia suggest cooling due to the decreasing influence of the Leeuwin Current at 14.5 and 11.8 kyr B.P. [*De Deckker et al.*, 2012] (Figure 6c), while opal flux records from E27-23 declined during the ACR, corresponding with a plateau in atmospheric CO_2, reduced upwelling and reduced sea surface temperatures [*Anderson et al.*, 2009]. The record of Antarctic temperature and deuterium (δD) from EPICA Dome C [*Parrenin et al.*, 2013] (Figures 6f and 6h) suggest temperatures declined during the ACR, while the sea salt flux from Dome C suggests the

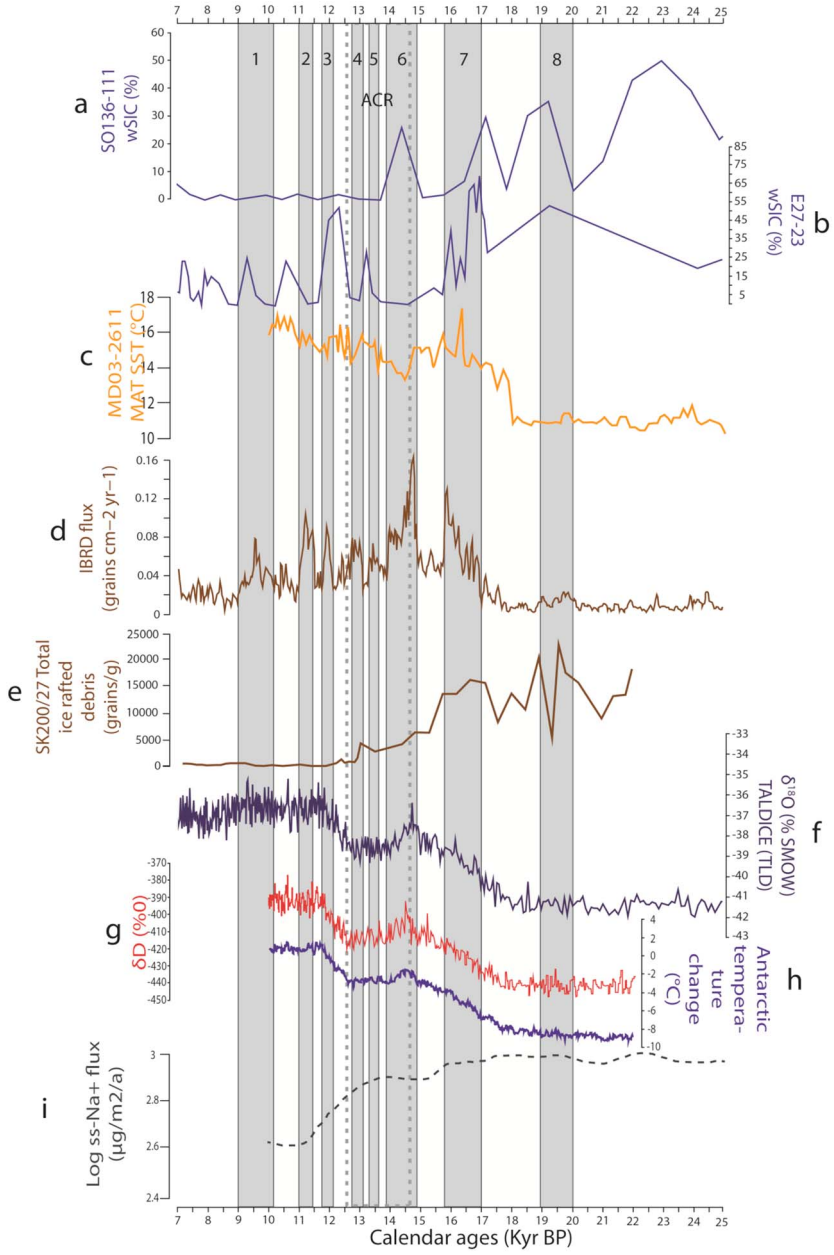

Figure 6. A comparison between the wSIC records from SO136-111 and E27-23 with the paleo records discussed in text. The paleo winter sea ice estimates for cores (a) SO136-111 and (b) E27-23 (solid blue lines) are plotted against the sea-surface temperature record from (c) *De Deckker et al.* [2012]. The Scotia Sea sediment flux reported by *Weber et al.* [2014] is shown in Figure 6d and the Indian Ocean IRD record of *Manoj et al.* [2013] is shown in Figure 6e (brown lines). The TALDICE δ^{18}O record from *Stenni et al.* [2010] is shown in Figure 6f (purple line). Figures 6g and 6h provide the record of δD from the EPICA Dome C ice core and Antarctic temperature change [*Parrenin et al.*, 2013]. (i) Also shown is the EPICA Dome C log sea salt sodium (ssNa) flux proxy for sea ice extent throughout the Indian Ocean sector [*Röthlisberger et al.*, 2010]. The Antarctic Ice Sheet Discharges (AID) first identified and described by *Weber et al.* [2014] are highlighted in light grey and labeled 1 through to 8. The Antarctic Cold Reversal, again as defined by *Weber et al.* [2014], is labeled and outlined with a dashed grey rectangle.

decline in sea ice extent throughout the Indian Ocean after the LGM halted during the ACR period [*Röthlisberger et al.*, 2010] (Figure 6i).

Our paleo estimates suggest winter sea ice cover increased within the southwest Pacific sector of the Southern Ocean over the sites of cores E27-23 and SO136-111 at 14.4 and 13.23 kyr B.P., respectively. A robust feature is the higher sea ice concentration estimated in the southern core (50% at 12.3 kyr B.P., for E27-23)

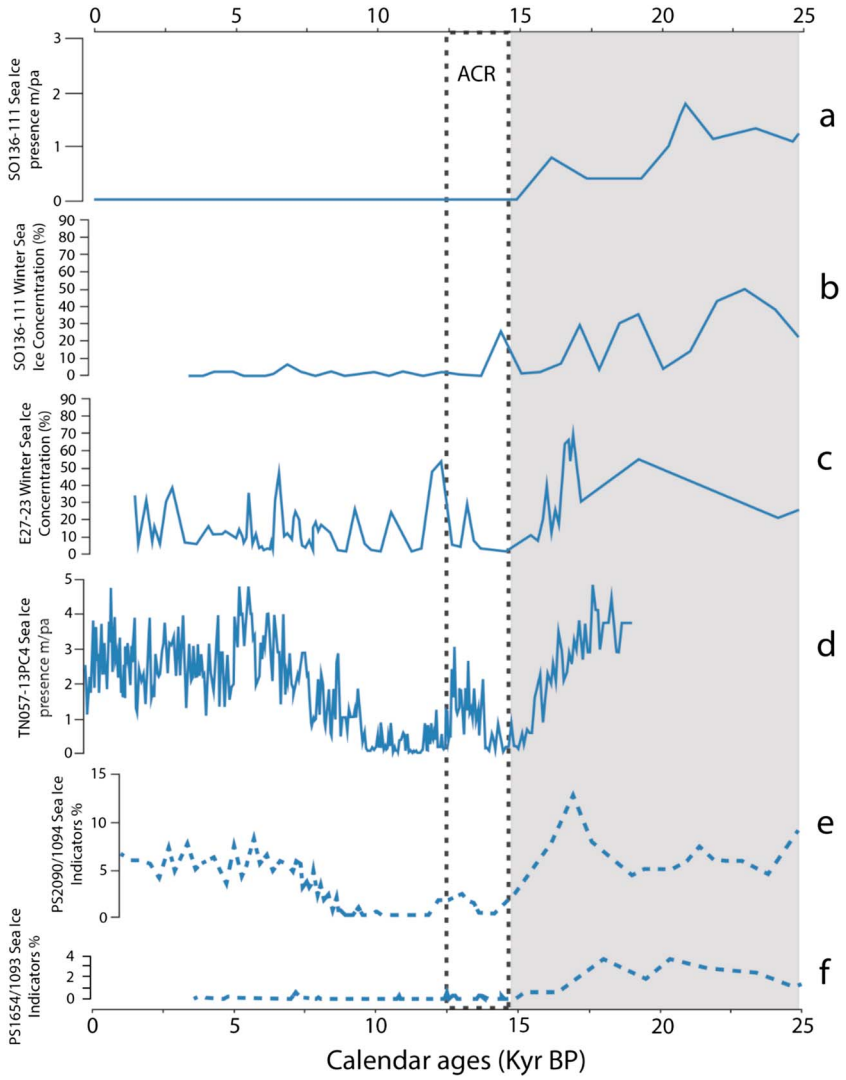

Figure 7. The paleo monthly sea ice cover from (a) *Crosta et al.* [2004] is compared with the winter sea ice concentration records for core (b) SO136-111 and (c) E27-23 (solid blue lines). The average monthly sea ice presence of *Divine et al.* [2010] (solid blue lines, Figure 7d) and the diatom sea ice indicator species of *Bianchi and Gersonde* [2004] (dashed blue lines, Figures 7e and 7f) from the South Atlantic sector are shown for comparison.

compared with the northern core (25% at 14.4 kyr B.P. for SO136-111). Yet the assumption of a constant radiocarbon reservoir age over time introduces a source of error into age models [*Hendy et al.*, 2011; *Cook and Keigwin*, 2015] and therefore contributes to the chronological uncertainties of our age models. Hence, resolving the ACR signal within both core records appears difficult given the uncertainties surrounding the independent age models for each core. Due to chronological uncertainties and the inconsistent timing for wSIC increases between E27-23 and SO136-111, we tentatively suggest an expansion of wSIC during the ACR (14.4 and 13.23 kyr BP) may have occurred throughout the southwest Pacific (Figures 6a and 6b). Our paleo winter sea ice estimates show that the sites of E27-23 and SO136-111 were both covered by unconsolidated winter sea ice during the interval covering previously estimated timings for the ACR in the Southern Ocean.

Interestingly, our paleo wSIC records for the southwest Pacific (cores SO136-111 and E27-23) contrast to those derived from the Atlantic sector of the Southern Ocean [*Bianchi and Gersonde*, 2004; *Divine et al.*, 2010] (Figures 7d–7f). While our sea ice records at the site of SO136-111 suggest sea ice cover during the ACR was greater than any time during the Holocene, ACR sea ice expansion within the Atlantic sector was no greater than estimated monthly sea ice cover during the early Holocene [*Bianchi and Gersonde*, 2004; *Divine et al.*, 2010]. Such regional differences are perhaps not surprising since Holocene sea ice expansion

within the south Atlantic may have resulted from a northern expansion and intensification of the Weddell Sea gyre circulation [*Bianchi and Gersonde*, 2004], which subsequently increased the northward transport of sea ice [*Divine et al.*, 2010].

4.1.3. The Holocene wSIC Increases Estimated From Core E27-23

Millennial-scale Holocene paleo climatic changes have been identified south of Australia [*Moros et al.*, 2009], the west Antarctic Peninsula [*Shevenell et al.*, 2011; *Etourneau et al.*, 2013], Palmer Deep [*Shevenell and Kennett*, 2002], within both coastal and inland Antarctic ice cores [*Masson et al.*, 2000] and from global paleo climatic records [*Mayewski et al.*, 2004]. The Holocene millennial scale cooling identified by *Shevenell and Kennett* [2002], *Mayewski et al.* [2004], *Shevenell et al.* [2011], and *Etourneau et al.* [2013] were attributed to short-term (and longer-term) variation in the intensity and/or latitudinal positioning of the westerly winds. For example, more southern and stronger westerly winds over the west Antarctic Peninsula bring more Circumpolar Deep Water (CDW) onto the shelf, warming sea surface temperatures and melting sea ice [*Shevenell et al.*, 2011]. We acknowledge that our wSIC record for E27-23 does not have the necessary resolution to adequately discuss millennial winter sea ice variation. However, we feel it is possible that our Holocene paleo wSIC record, which documents unconsolidated (i.e., wSIC $>$ 15%) wSIC roughly every 1 kyr, (Figure 6b) could suggest southwestern Pacific sea ice cover may have increased during periods of climatic cooling identified by *Masson et al.* [2000], *Shevenell and Kennett* [2002], and *Shevenell et al.* [2011].

5. Conclusions

We provide the first quantitative paleo winter sea ice estimates for marine sediment cores E27-23 and SO136-111, extending our paleoceanographic knowledge of the southwest Pacific sector of the Southern Ocean. To complement our refinement of the paleo sea ice record, we proposed and applied an extension of the available satellite record of sea ice concentration according to a time series analysis on 30 years of sea ice concentration data for each sector of the Southern Ocean.

During glacial stages unconsolidated winter sea ice was present at 54°S within the southwest Pacific sector of the Southern Ocean. The glacial winter sea ice expansion was concomitant with a northern migration of the ACC, PF, SAF, and/or STF. GAM-based paleo wSIC estimates suggest winter sea ice might have expanded during the ACR and Holocene within the currently open ocean region of the southwest Pacific sector of the Southern Ocean. The sea ice concentration increases documented during the ACR are consistent with a northern migration of regional oceanic fronts (PF, SAF, and STF), a northern migration of the ACC, and reduced influence of the Leeuwin Current to the south of Australia. The wSIC increases documented during the ACR, and the Holocene are consistent with theories suggesting a latitudinal shift and/or increase in the westerly wind field were the causal mechanisms for documented climatic changes. However, we cannot contribute any clarification regarding the controversial role potentially played by shifts in the positioning or intensity of the westerly wind field during past climatic shifts. At no stage did our cores record the existence of summer sea ice cover up to 56°S, and thus, a strong seasonal sea ice growth and retreat cycle has been maintained over cooling expansions for the last 15 kyr B.P. The influence on oceanic and atmospheric fronts as a result of such large seasonal differences cannot be determined here but should be considered in paleo modeling scenarios.

Acknowledgments

All of the data provided within Appendices A through to F are available via the Australian Antarctic Division metadata records (10.4225/15/546C10AD26A7D). This research was funded by the Australian Government through the provision of an Australian Postgraduate Award granted to Alexander Ferry. We are also grateful for the input and assistance from R. Hyndman in the application of ARIMA using the R package "forecast." The work on core E27-23 was originally undertaken through the Antarctic Cooperative Research Centre's Palaeoenvironments Program and was completed via support from ASAC grant 2534 to PQ and LA, AINSE Grant 2572 to PQ and WH, and additional support from the University of Tasmania's School of Earth Sciences and the Australian Government's Cooperative Research Centers Program through the Antarctic Climate and Ecosystems Cooperative Research Centre (ACE CRC). Technical support from L. Robertson and D. Roberts at the University of Tasmania is acknowledged. Lloyd Burckle (LDEO) originally provided radiocarbon dates for three intervals in the core through the laboratory of J. Lynch-Stieglitz (LDEO). T. Janecek, M. Curran, and S. Nielsen (former curators of the Florida State University Antarctic Core Repository) assisted us with sampling requests for E27-23. We thank M. Gagan, H. Scott-Gagan, and J. Cali for the use of the mass spectrometer at ANU. We are thankful for the assistance of S. Rintoul and S. Sokolov of CSIRO Marine and Atmospheric Research with oceanography, R. Massom of ACE CRC with sea ice cover, and R. Anderson of Lamont Doherty Earth Observatory for palaeoceanographic discussions.

References

Anderson, R. F., S. Ali, L. I. Bradtmiller, S. H. H. Nielsen, M. Q. Fleisher, B. E. Anderson, and L. H. Burckle (2009), Wind-driven upwelling in the Southern Ocean and the deglacial rise in atmospheric CO_2, *Science*, *323*, 1443–1448.

Armand, L. K., and A. Leventer (2010), Palaeo sea ice distribution and reconstruction derived from the geological record, in *Sea Ice*, 2nd ed., edited by D. N. Thomas and G. S. Dieckmann, chap. 13, pp. 469–529, Wiley-Blackwell, Oxford, U. K.

Bianchi, C., and R. Gersonde (2004), Climate evolution at the last deglaciation: The role of the Southern Ocean, *Earth Planet. Sci. Lett.*, *228*, 407–424.

Birks, H. J. B., J. M. Line, S. Juggins, A. C. Stevenson, and C. J. F. ter Braak (1990), Diatoms and pH reconstruction, *Philos. Trans. R. Soc. London B*, *327*, 263–278.

Blaauw, M. (2010), Methods and code for 'classical' age-modelling of radiocarbon sequences, *Quat. Geochronol.*, *5*, 512–518.

Brandon, M. A., R. R. Cottier, and F. Nilsen (2010), Sea ice and oceanography, in *Sea Ice*, 2nd ed., edited by D. N. Thomas and G. S. Dieckmann, pp. 79–111, Wiley-Blackwell, Oxford, U. K.

Bronk Ramsey, C. (2009), Bayesian analysis of radiocarbon dates, *Radiocarbon*, *51*, 337–360.

Butzin, M., M. Prange, and G. Lohmann (2005), Radiocarbon simulations for the glacial ocean: The effects of wind stress, Southern Ocean sea ice and Heinrich events, *Earth Planet. Sci. Lett.*, *235*, 45–61.

Cassidy, D. S., F. A. Kaharoeddin, I. Zemmels, and M. B. Knapp (1977), USNS ELTANIN. An inventory of core location data with core location maps and cruise 55 core descriptions, *Tech. Rep. 44*, Antarct. Res. Facil., Tallahassee, Fla.

Cavalieri, D. J., C. L. Parkinson, P. Gloersen, and H. J. Zwally (1996), Sea Ice Concentrations from Nimbus-7 SMMR and DMSP SSM/I-SSMIS Passive Microwave Data, Version 1. Boulder, Colorado USA. NASA National Snow and Ice Data Center Distributed Active Archive Center, doi:10.5067/8GQ8LZQVL0VL. [Updated yearly.]

Comiso, J. (2000), Bootstrap sea ice concentrations from Nimbus-7 SMMR and DMSP SSM/I-SSMIS, Version 2, Natl. Snow and Ice Data Cent., Boulder, Colo.

Cook, M. S., and L. D. Keigwin (2015), Radiocarbon profiles of the NW Pacific from the LGM and deglaciation: Evaluating ventilation metrics and the effect of uncertain surface reservoir ages, *Paleoceanography*, *30*, 174–195, doi:10.1002/2014PA002649.

Comiso, J. C. (2010), Variability and trends of the global sea ice cover, in Sea Ice, 2nd ed., edited by D. N. Thomas and G. S. Dieckmann, chap. 6, pp. 247–282, Wiley-Blackwell, Oxford, U. K.

Crosta, X., J.-J. Pichon, and L. H. Burckle (1998), Application of modern analog technique to marine Antarctic diatoms: Reconstruction of maximum sea-ice extent at the Last Glacial Maximum, *Paleoceanography*, *13*, 284–297, doi:10.1029/98PA00339.

Crosta, X., A. Shemesh, M.-E. Salvignac, H. Gildor, and R. Yam (2002), Late Quaternary variations of elemental ratios (C/Si and N/Si) in diatom-bound organic matter from the Southern Ocean, *Deep Sea Res., Part II*, *49*, 1939–1952.

Crosta, X., A. Sturm, L. Armand, and J.-J. Pichon (2004), Late Quaternary sea ice history in the Indian sector of the Southern Ocean as recorded by diatom assemblages, *Mar. Micropaleontol.*, *50*, 209–223.

Crosta, X., A. Shemesh, J. Etourneau, R. Yam, I. Billy, and J. J. Pichon (2005), Nutrient cycling in the Indian sector of the Southern Ocean over the last 50,000 years, *Global Biogeochem. Cycles*, *19*, GB3007, doi:10.1029/2004GB002344.

De Deckker, P., M. Moros, K. Perner, and E. Jansen (2012), Influence of the tropics and southern westerlies on glacial interhemispheric asymmetry, *Nat. Geosci.*, *5*, 266–269.

Dieckmann, G. S., and H. H. Hellmer (2010), The importance of sea ice: An overview, in *Sea Ice*, 2nd ed., edited by D. N. Thomas and G. S. Dieckmann, pp. 1–22, Wiley-Blackwell, Oxford, U. K.

Divine, D. V., N. Koç, E. Isaksson, S. Nielsen, X. Crosta, and F. Godtliebsen (2010), Holocene Antarctic climate variability from ice and marine sediment cores: Insights on ocean–atmosphere interaction, *Quat. Sci. Rev.*, *29*, 303–312.

Etourneau, J., et al. (2013), Holocene climate variations in the western Antarctic Peninsula: Evidence for sea ice extent predominantly controlled by changes in insolation and ENSO variability, *Clim. Past*, *9*, 1431–1446.

Ferry, A. J., T. Prvan, B. Jersky, X. Crosta, and L. K. Armand (2015), Statistical modeling of Southern Ocean marine diatom proxy and winter sea ice data: Model comparison and developments, *Prog. Oceanogr.*, *131*, 100–112.

Fink, D., et al. (2004), The ANTARES AMS facility at ANSTO, *Nucl. Instrum. Methods Phys. Res., Sect. B*, *223–224*, 109–115.

Gersonde, R., and U. Zielinski (2000), The reconstruction of late Quaternary Antarctic sea ice distribution—The use of diatoms as a proxy for sea-ice, *Palaeogeogr. Palaeoclimatol. Palaeoecol.*, *162*, 263–286.

Gersonde, R., X. Crosta, A. Abelmann, and L. Armand (2005), Sea-surface temperature and sea ice distribution of the Southern Ocean at the EPILOG Last Glacial Maximum—A circum-Antarctic view based on siliceous microfossil records, *Quat. Sci. Rev.*, *24*, 869–896.

Gloersen, P., W. J. Campbell, D. J. Cavalieri, J. C. Comiso, C. L. Parkinson, and H. J. Zwally (1992), *Arctic and Antarctic Sea Ice, 1978–1987, Satellite Passive-Microwave Observations and Analysis*, *NASA Spec. Publ. 511*, 289 pp., Natl. Aeronaut. and Space Admin., Washington, D. C.

Goosse, H., D. M. Roche, A. Mairesse, and M. Berger (2013), Modelling past sea ice changes, *Quat. Sci. Rev.*, *79*, 191–206.

Hammer, Ø., D. A. T. Harper, and P. D. Ryan (2001), PAST: Paleontological statistics software package for education and data analysis, *Palaeontol. Electron.*, *4*, 4.

Hendy, I. L., L. Dunn, A. Schimmelmann, and D. K. Pak (2011), Millennial-scale surface water mass radiocarbon reservoir age changes recorded on the California Margin, Abstract PP52A-04 presented at 2011 Fall Meeting, AGU.

Hill, M. O. (1973), Diversity and evenness: A unifying notation and its consequences, *Ecology*, *54*, 427–432.

Hua, Q., G. E. Jacobsen, U. Zoppi, E. M. Lawson, A. A. Williams, A. M. Smith, and M. J. McGann (2001), Progress in radiocarbon target preparation at the ANTARES AMS centre, *Radiocarbon*, *43*, 275–282.

Hyndman, R. (2014), Forecast. R package version 5.4. [Available at http://cran.rproject.org/web/packages/forecast/index.html.]

Juggins, S. (2014), Rioja: Analysis of Quaternary Science Data, R package version 0.9-3. [Available at http://cran.r-project.org/web/packages/rioja/index.html.]

Kohfeld, K. E., R. M. Graham, A. M. de Boer, L. C. Sime, E. W. Wolff, C. Le Quéré, and L. Bopp (2013), Southern Hemisphere westerly wind changes during the Last Glacial Maximum: Paleo-data synthesis, *Quat. Sci. Rev.*, *68*, 76–95.

Lisiecki, L. E., and M. E. Raymo (2005a), A Pliocene-Pleistocene stack of 57 globally distributed benthic δ18O records, *Paleoceanography*, *20*, PA1003, doi:10.1029/2004PA001071.

Lisiecki, L. E., and M. E. Raymo (2005b), LR04 Global Pliocene-Pleistocene Benthic δ18O stack, IGBP PAGES/world data center for paleoclimatology data contribution series #2005-008, NOAA/NGDC Paleoclimatol. Program, Boulder, Colo.

Manoj, M. C., M. Thamban, A. Sahana, R. Mohan, and K. Mahender (2013), Provenance and temporal variability of ice rafted debris in the Indian sector of the Southern Ocean during the last 22,000 years, *J. Earth Syst. Sci.*, *122*, 491–501.

Martinson, D. G. (2012), Antarctic circumpolar current's role in the Antarctic ice system: An overview, *Palaeogeogr. Palaeoclimatol. Palaeoecol.*, *335-336*, 71–74.

Massom, R., P. Reid, S. Stammerjohn, B. Raymond, A. Fraser, and S. Ushio (2013), Change and variability in East Antarctic sea ice seasonality, 1979/80–2009/10, *PLoS One*, *8*, doi:10.1371/journal.pone.0064756.

Masson, V., et al. (2000), Holocene climate variability in Antarctica based on 11 ice-core isotopic records, *Quat. Res.*, *54*, 348–358.

Mayewski, P. A., et al. (2004), Holocene climate variability, *Quat. Res.*, *62*, 243–255.

Mazaud, A., E. Michel, F. Dewilde, and J. L. Turon (2010), Variations of the Antarctic Circumpolar Current intensity during the past 500 ka, *Geochem. Geophys. Geosyst.*, *11*, Q08007, doi:10.1029/2010GC003033.

Moros, M., P. De Deckker, E. Jansen, K. Perner, and R. J. Telford (2009), Holocene climate variability in the Southern Ocean recorded in a deep-sea sediment core off South Australia, *Quat. Sci. Rev.*, *28*, 1932–1940.

Neil, H. L., L. Carter, and M. Y. Morris (2004), Thermal isolation of Campbell Plateau, New Zealand, by the Antarctic Circumpolar Current over the past 130 kyr, *Paleoceanography*, *19*, PA4008, doi:10.1029/2003PA000975.

Newnham, R. M., D. J. Lowe, T. Giles, and B. V. Alloway (2007), Vegetation and climate of Auckland, New Zealand, since ca. 32 000 cal. yr ago: Support for an extended LGM, *J. Quat. Sci.*, *22*, 517–534.

Paillard, D., L. Labeyrie, and P. Yiou (1996), Macintosh program performs time-series analysis, *Eos Trans. AGU*, *77*, 379, doi:10.1029/96EO00259.

Parkinson, C. L., and D. J. Cavalieri (2012), Antarctic sea ice variability and trends, 1979–2010, *Cryosphere*, *6*, 871–880.

Parrenin, F., V. Masson-Delmotte, P. Köhler, D. Raynaud, D. Paillard, J. Schwander, C. Barbante, A. Landais, A. Wegner, and J. Jouzel (2013), Synchronous change of atmospheric CO2 and Antarctic temperature during the last deglacial warming, *Science*, *339*, 1060–1063.
Putnam, A. E., G. H. Denton, J. M. Schaefer, D. J. A. Barrell, B. G. Andersen, R. C. Finkel, R. Schwartz, A. M. Doughty, M. R. Kaplan, and C. Schlüchter (2010), Glacier advance in southern middle-latitudes during the Antarctic Cold Reversal, *Nat. Geosci.*, *3*, 700–704.
Recasens, C., D. Ariztegui, N. I. Maidana, B. Zolitschka, and the PASADO Science Team (2015), Diatoms as indicators of hydrological and climatic changes in Laguna Potrok Aike (Patagonia) since the Late Pleistocene, *Palaeogeogr. Palaeoclimatol. Palaeoecol.*, *417*, 309–319.
Reimer, P. J., et al. (2013), IntCal13 and Marine13 radiocarbon age calibration curves 0–50,000 years cal BP, *Radiocarbon*, *55*, 1869–1887.
Röthlisberger, R., X. Crosta, N. J. Abram, L. Armand, and E. W. Wolff (2010), Potential and limitations of marine and ice core sea ice proxies: An example from the Indian Ocean sector, *Quat. Sci. Rev.*, *29*, 296–302.
Schneider-Mor, A., R. Yam, C. Bianchi, M. Kunz-Pirrung, R. Gersonde, and A. Shemesh (2005), Diatom stable isotopes, sea ice presence and sea surface temperature records of the past 640 ka in the Atlantic sector of the Southern Ocean, *Geophys. Res. Lett.*, *32*, L10704, doi:10.1029/2005GL022543.
Schweitzer, P. N. (1995), Monthly average polar sea-ice concentration: U.S. Geological Survey digital data series, DDS-27, U.S. Geological Surv., Reston, Va. [Available http://pubs.usgs.gov/dds/dds27/.]
Shevenell, A. E., and J. P. Kennett (2002), Antarctic Holocene climate change: A benthic foraminiferal stable isotope record from Palmer Deep, *Paleoceanography*, *17*(2), 1019, doi:10.1029/2000PA000596.
Shevenell, A. E., A. E. Ingalls, E. W. Domack, and C. Kelly (2011), Holocene Southern Ocean surface temperature variability west of the Antarctic Peninsula, *Nature*, *470*, 250–254.
Shulmeister, J., et al. (2004), The Southern Hemisphere westerlies in the Australasian sector over the last glacial cycle: A synthesis, *Quat. Int.*, *118–119*, 23–53.
Simmonds, I. (2015), Comparing and contrasting the behavior of Arctic and Antarctic sea ice over the 35 year period 1979–2013, *Ann. Glaciol.*, *56*, 18–28, doi:10.3189/2015AoG69A909.
Sokolov, S., and S. R. Rintoul (2009), Circumpolar structure and distribution of the Antarctic Circumpolar Current fronts: 1. Mean circumpolar paths, *J. Geophys. Res.*, *114*, C11018, doi:10.1029/2008JC005108.
Spolaor, A., P. Vallelonga, J. Gabrieli, N. Kehrwald, V. Turetta, G. Cozzi, L. Poto, J. M. C. Plane, C. Boutron, and C. Barbante (2013), Speciation analysis of iodine and bromine at picogram-per-gram levels in polar ice, *Anal. Bioanal. Chem.*, *405*, 647–654.
Stammerjohn, S., R. Massom, D. Rind, and D. Martinson (2012), Regions of rapid sea ice change: An inter-hemispheric seasonal comparison, *Geophys. Res. Lett.*, *39*, L06501, doi:10.1029/2012GL050874.
Stenni, B., V. Masson-Delmotte, S. Johnsen, J. Jouzel, A. Longinelli, E. Monnin, R. Röthlisberger, and E. Selmo (2001), An oceanic cold reversal during the last deglaciation, *Science*, *293*, 2074–2077.
Stenni, B., et al. (2010), Expression of the bipolar see-saw in Antarctic climate records during the last deglaciation, *Nat. Geosci.*, *4*, 46–49, doi:10.1038/NGEO1026.
Stern, J., and L. E. Lisiecki (2014), Termination 1 timing in radiocarbon-dated regional benthic δ^{18}O stacks, *Paleoceanography*, *29*, 1127–1142, doi:10.1002/2014PA002700.
Stuiver, M., and P. J. Reimer (1993), Extended ^{14}C database and revised CALIB radiocarbon calibration program, *Radiocarbon*, *35*, 215–230.
Telford, R. J., and H. J. B. Birks (2011), Effect of uneven sampling along an environmental gradient on transfer-function performance, *J. Paleolimnol.*, *46*, 99–106.
Weber, M. E., et al. (2014), Millennial-scale variability in Antarctic ice-sheet discharge during the last deglaciation, *Nature*, *510*, 134–138, doi:10.1038/nature13397.
Wood, S. (2014), mgcv: Mixed GAM Computation Vehicle with GCV/AIC/REML Smoothness Estimation, R package version 1.8-5. [Available at http://cran.r841project.org/web/packages/mgcv/index.html.]